ARTICLE

Open Access

Observation of the hyperfine structure and anticrossings of hyperfine levels in the luminescence spectra of $LiYF_4$:Ho^{3+}

Kirill N. Boldyrev [1], Boris Z. Malkin [2] and Marina N. Popova [1]✉

Abstract

Resolved hyperfine structure and narrow inhomogeneously broadened lines in the optical spectra of a rare-earth-doped crystal are favorable for the implementation of various sensors. Here, a well-resolved hyperfine structure in the photoluminescence spectra of $LiYF_4$:Ho single crystals and the anticrossings of hyperfine levels in a magnetic field are demonstrated using a self-made setup based on a Bruker 125HR high-resolution Fourier spectrometer. This is the first observation of the resolved hyperfine structure and anticrossing hyperfine levels in the luminescence spectra of a crystal. The narrowest spectral linewidth is only 0.0022 cm^{-1}. This fact together with a large value of the magnetic g factor of several crystal-field states creates prerequisites for developing magnetic field sensors, which can be in demand in modern quantum information technology devices operating at low temperatures. Very small random lattice strains characterizing the quality of a crystal can be detected using anticrossing points.

Introduction

Crystals doped with rare-earth (RE) ions exhibit very narrow homogeneous and inhomogeneous linewidths of the $4f^N–4f^N$ optical transitions, since the $4f^N$ electronic shell is well shielded from the crystalline environment by the filled 5s and 5p shells. The narrow-line spectra of transitions within the $4f^N$ shell of triply ionized RE elements cover the entire visible and infrared range. RE-doped materials are widely used as laser media, phosphors, scintillators, in solar cells, etc. Nowadays, RE-based luminescence thermometry is successfully developing, demonstrating a wide working temperature range, high thermal sensitivity, and spatial resolution[1,2]. Over the past decade, significant progress has been achieved in the application of RE-doped crystals for quantum information processing, which is based on the use of electronic-nuclear hyperfine levels[3–8]. Information on the hyperfine and superhyperfine interactions, isotopic effects,

inhomogeneous line shapes, and random lattice strains in a crystal is essential for applications in modern quantum technologies. It can be acquired using high-resolution optical spectroscopy. High-resolution studies also reveal the narrowest spectral lines, which are favorable for sensor applications.

A series of high-resolution studies of RE materials has been performed using absorption or photoluminescence (PL) excitation spectroscopies. Hyperfine[7,9–25], super-hyperfine[24], and isotope[23–30] structures, as well as specific line shapes imposed by random lattice strains[23,31,32] and the hyperfine level anticrossings in a magnetic field[33] were observed in optical absorption spectra of a number of RE-doped crystals. We are not aware of any broadband high-resolution study of the luminescence spectra of RE-doped crystals, as well as of a resolved hyperfine structure in these spectra. However, the luminescence spectra open up additional possibilities, such as, e.g., the study of very small and/or highly diluted samples or the development of new types of remote sensors. Here, we present the results of a high-resolution study of broadband PL spectra of $LiYF_4$:Ho crystals in a magnetic field.

Correspondence: Marina N. Popova (popova@isan.troitsk.ru)
[1]Institute of Spectroscopy, Russian Academy of Sciences, Troitsk, Moscow 108840, Russia
[2]Kazan Federal University, Kazan 420008, Russia

Results

Photoluminescence of LiYF$_4$:Ho^{3+} in zero magnetic field: hyperfine structure

Lithium yttrium fluoride crystals, LiYF$_4$, exhibit the luminescence from many optically excited levels of RE ions doped into this crystal, in a wide spectral range. PL of a LiYF$_4$:Ho^{3+} (0.1 at. %) crystal was excited by the wavelength 638.3 nm of a diode laser. This excitation wavelength corresponds to the transition from the ground state to the upper crystal-field (CF) level of the $^5F_5$ multiplet of the Ho^{3+} ion (see Supplementary Fig. S1). High-resolution PL spectra were acquired on an experimental setup built on the basis of a Bruker IFS 125HR high-resolution Fourier spectrometer (Fig. 1a and Methods).

Figure 1b shows the low-temperature PL spectrum of LiYF$_4$:Ho^{3+} (0.1 at. %), in the whole spectral range studied. The observed optical manifolds are identified in accordance with the scheme given in the inset. Figure 1c, d presents the spectral manifolds $^5I_6 \rightarrow {}^5I_7$ and $^5I_7 \rightarrow {}^5I_8$, respectively, in extended scales as examples. At low temperatures, only lowest-energy levels of the $^5I_6$ and $^5I_7$ excited CF multiplets are populated after the laser excitation. The lines in the low-frequency part of the luminescent manifolds correspond to transitions to the upper levels of the final CF multiplets, broadened due to phonon relaxation to underlying levels[9]. In the high-frequency parts of the manifolds, many lines with well-resolved hyperfine structure are observed, as insets of Fig. 1c, d show.

The resolved hyperfine structure in optical absorption spectra of LiYF$_4$:Ho^{3+} was discovered[9] and studied in detail[9–12] earlier. The CF energy levels of Ho^{3+} are characterized by the one-dimensional Γ_1 and Γ_2 and two-dimensional Γ_{34} irreducible representations (IR) of the S_4 point symmetry group of the holmium site in LiYF$_4$. Table 1 lists the energies and symmetries (IRs) of several CF levels of Ho^{3+} in LiYF$_4$ (relevant for further discussion), determined from the analysis of polarized absorption and luminescence spectra, using the selection rules[11,12] (see Supplementary Table S1). An extended table of CF levels is presented in Supplementary Table S3. The data obtained are consistent with the results of previous studies[9–12], with one exception. Namely, we did not find the level 11,242.4 cm^{-1} ($^5I_5$)[12], but demonstrated the level 11,254.0 cm^{-1}, which is absent in ref. [12]. Figure 2 illustrates this. We note that the allowed ED transition $^5I_8$ (1, Γ_{34}) $\rightarrow {}^5I_5$ (4, Γ_2) [11,254 cm^{-1}] is nevertheless very weak and can easily be missed if for some reason (higher holmium concentration, insufficient spectral resolution) the spectral lines are broadened.

In a zero magnetic field, the Γ_{34} CF levels possess an eight-component equidistant magnetic hyperfine structure resulting from the interaction of 4f electrons with the magnetic moment of the holmium nucleus with spin $I = 7/2$. Each hyperfine component is doubly degenerate, the states $|\Gamma_3, m>$ and $|\Gamma_4, -m>$ have the same energy (here, m is the component of nuclear moment I along the crystallographic c axis, $-7/2 \le m \le 7/2$)[9,12]. For the Γ_1 and Γ_2 non-degenerate electronic CF states magnetic HFS is forbidden in the first approximation. Electric quadrupole and pseudoquadrupole (magnetic dipole in the second approximation) hyperfine interactions split Γ_1 and Γ_2 singlets into four nonequidistant hyperfine sublevels and lead to nonequidistance in Γ_{34} hyperfine manifolds[10].

In the luminescence spectra, HFS is observed in other spectral regions compared to absorption spectra, in particular, at telecommunication wavelengths around 1.5 μm (transitions $^5F_5 \rightarrow {}^5I_6$ and $^5I_5 \rightarrow {}^5I_7$), which can be used, for example, to implement remote magnetic field sensors. For sensor applications, such parameters as the luminescence linewidth and sensitivity of the line position to perturbations are important.

Isotopic structure in the photoluminescence spectra of ^{7}Li$_{1-x}$^{6}Li$_x$YF$_4$:Ho^{3+} and linewidths of hyperfine components

Figure 3a, b shows the absorption and PL spectra, respectively, of ^{7}Li$_{1-x}$^{6}Li$_x$YF$_4$:Ho^{3+} single crystals with different lithium isotope compositions, in the region of the optical transition between the $^5I_7$ Γ_{34} (5155.7 cm^{-1}) and $^5I_8$ Γ_2 (6.85 cm^{-1}) CF levels of Ho^{3+}. An identical fine structure of the hyperfine components is clearly observed in the absorption and PL spectra if $x \ne 0$. Earlier, the structure observed in the absorption spectra was unambiguously ascribed to the isotopic disorder in the lithium sublattice[26,27]. Because of the difference in masses of the lithium isotopes, the amplitudes of their zero-field vibrations differ, leading to different equilibrium positions of the nearest fluorine ions (through the anharmonicity of vibrations) and, thus, to the dependence of the crystal field for the Ho^{3+} ion on the lithium isotope composition in its nearest surrounding[26]. Evidently, the origin of the fine structure of the hyperfine components in the PL spectra is the same. Figure 3c gives an example of such isotopic structure in the PL line corresponding to a singlet–singlet transition.

In what follows, we study PL spectra of LiYF$_4$:Ho^{3+} in an external magnetic field. To avoid complexities associated with the isotopic structure, we use a monoisotopic ^{7}LiYF$_4$:Ho^{3+} crystal. Preliminarily we investigated the widths of the PL lines in a zero magnetic field. Here, a remark is necessary concerning the resolution. The instrumental function of a Fourier spectrometer has the form $f_L(\sigma) = \frac{\sin x}{x}$, $x = 4\pi L\sigma$, where σ is the wavenumber and L is the maximal displacement of a moving mirror in a Michelson interferometer. The distance between the first zeros of $f_L(\sigma)$ equals $\delta\sigma = 1/2\,L$ (0.001 cm^{-1} in our case) and is indicated as "resolution" in an instrument manual. The full width at half maximum (FWHM) of f_L is

Fig. 1 PL spectrum of LiYF$_4$:Ho^{3+} (0.1 at. %): $T = 6$ K, $B = 0$; $\lambda_{ex} = 638.3$ nm. a Setup: 1—cryostat with magnetic coils (gray hatched), 1a—temperature controller, 1b—current source for magnetic coils; 2—temperature-stabilized diode laser, 2a—temperature controller and current source for laser; 3—PL module; 4—Fourier spectrometer; 5—PL registration module, 5a—preamplifier and an analog to digital converter; 6—workstation for spectra calculation and automatic control of magnetic field and temperature. **b** The whole spectral region studied. Identified intermultiplet transitions of Ho^{3+} as well as the $^4I_{13/2} \rightarrow {}^4I_{15/2}$ transition of Er^{3+} trace impurity are indicated. Inset presents the scheme of energy levels of Ho^{3+}; the observed transitions are shown by arrows. **c** $^5I_6 \rightarrow {}^5I_7$ and **d** $^5I_7 \rightarrow {}^5I_8$ luminescent transitions. Insets show the spectral lines highlighted in blue on an enlarged scale. The numbers $n_i \rightarrow n_f$ indicate the initial and final levels of the corresponding transition, numbered from the lowest level in the CF multiplet (Table 1).

Table 1 Information on CF levels of Ho^{3+} in $LiYF_4$:Ho^{3+}.

	n	IR	E (cm^{-1})	Δ_{HFS} (cm^{-1})	$g_{||}$
$^5F_5$	3	Γ_1	15,512.7		
	2	Γ_{34}	15,495.4	0.034	-4.2
	1	Γ_2	15,489.4		
$^5I_5$	5	Γ_1	11,255.6		
	4	Γ_2	11,254.0		
	3	Γ_{34}	11,249.9	0.069	-2.8
	2	Γ_1	11,247.2		
	1	Γ_{34}	11,241.6	0.178	8.1
$^5I_6$	6	Γ_1	8697.4		
	5	Γ_2	8687.75		
	4	Γ_{34}	8685.9	0.095	6.4
	3	Γ_{34}	8680.3	0.015	1.0
	2	Γ_1	8673.4		
	1	Γ_2	8670.9		
$^5I_7$	6	Γ_1	5206.1		
	5	Γ_{34}	5184.7	0.131	−10.5
	4	Γ_2	5163.3		
	3	Γ_1	5162.8		
	2	Γ_{34}	5155.75	0.088	6.8
	1	Γ_2	5152.3		
$^5I_8$	3	Γ_2	23.3		
	2	Γ_2	6.85		
	1	Γ_{34}	0	0.147	−13.3

Irreducible representations IRs, crystal-field energies E (cm^{-1}), average intervals of the magnetic hyperfine structure Δ_{HFS} (cm^{-1}), and g factors of Γ_{34} doublets, obtained from the analysis of the optical spectra of $LiYF_4$:Ho^{3+} (0.1 at. %).

Fig. 2 $^5I_5$ CF levels with resolved HFS. The π- ($\mathbf{k} \perp c$, $\mathbf{E}||c$; black trace) and σ- ($\mathbf{k} \perp c$, $\mathbf{E} \perp c$; red trace) polarized absorption spectra of a $LiYF_4$:Ho^{3+} (0.1 at. %) single crystal at the temperature 3.5 K in zero magnetic field. $\delta\sigma = 1/2\,L = 0.01$ cm^{-1} (L is the maximal displacement of a moving mirror in the Fourier spectrometer).

0.002 to 0.004 cm^{-1} (for comparison, the smallest line-width observed in the absorption spectra of this crystal is 0.012 cm^{-1}). The $^5I_6 \rightarrow {}^5I_7$ transitions, inaccessible in absorption, exhibit the narrowest spectral lines. The PL linewidth of 0.002 cm^{-1} observed here is, as far as we know, the smallest inhomogeneous linewidth ever observed in the luminescence spectra of crystals.

Photoluminescence of $^7LiYF_4$:Ho^{3+} in an external magnetic field $B||c$

The twofold degeneracy of the hyperfine states $|\Gamma_3, m>$ and $|\Gamma_4, -m>$ is lifted in an external magnetic field parallel to the c axis of the crystal, $\mathbf{B}||c$. The electronic Zeeman energies are equal to $\pm g_{||}\mu_B B/2$, where $\mu_B = 0.4669$ cm^{-1}T^{-1} is the Bohr magneton and $g_{||}$ is the g factor of a doublet. Figure 5 shows HFS in a magnetic field $\mathbf{B}||c$ for two PL lines of $^7LiYF_4$:Ho^{3+} (0.1 at. %) starting from the $^5I_5$ Γ_{34} doublet at 11,241.6 cm^{-1}. The line 6089.3 cm^{-1} has the $^5I_7$ Γ_2 singlet at 5152.3 cm^{-1} as a terminal level, its splitting is governed by the g factor $g_{||} = 8.1$ of the $^5I_5$ Γ_{34} (11,241.6) doublet. Magnetic g factors of several Γ_{34} doublets given in Table 1 were determined experimentally by analyzing the splitting of PL lines corresponding to transitions between a given doublet and a singlet. We note that the g factor is proportional to the hyperfine interval Δ_{HFS} (ref. [9]): $|g_{||}| = 2g_0\Delta_{HFS}/A_J$, where g_0 is the Lande factor and A_J is the magnetic hyperfine constant (see Supplementary information, Eqs. S5, S9, and S10).

The line 6085.85 cm^{-1} ends at the $^5I_7$ Γ_{34} (5155.75) doublet, and the hyperfine interval in HFS of this line is a sum of the hyperfine intervals in the initial $^5I_5$ Γ_{34} (11,241.6) and final $^5I_7$ Γ_{34} (5155.75) doublets of the transition but the splitting follows the sum of g factors of the involved levels,

0.6$\delta\sigma$. The measured line shape is a convolution of a real line shape and the instrumental function f_L. The line shape practically does not change down to $W = 2\delta\sigma$ (W is FWHM of the studied spectral line). At $W = \delta\sigma$, weak additional maxima appear on the line wings, and in the case of the Loretzian line shape, FWHM of the convolution exceeds by 10% FWHM of the original line[34] (see Supplementary Fig. S3).

Figure 4 shows several PL lines of the $^5I_6 \rightarrow {}^5I_7$ transition in Ho^{3+}:$^7LiYF_4$. The lines represented in Fig. 4a, b correspond to the transitions from the lowest in the $^5I_6$ multiplet Γ_1 and Γ_2 CF singlets, respectively, to the $^5I_7$ Γ_{34} (5155.75 cm^{-1}) doublet and reflect HFS of the latter. The four-component line of Fig. 4c originates from a singlet–singlet transition.

To find the correct linewidths of the hyperfine components, we approximated the observed spectra with sets of Loretzians. The FWHM thus obtained range from
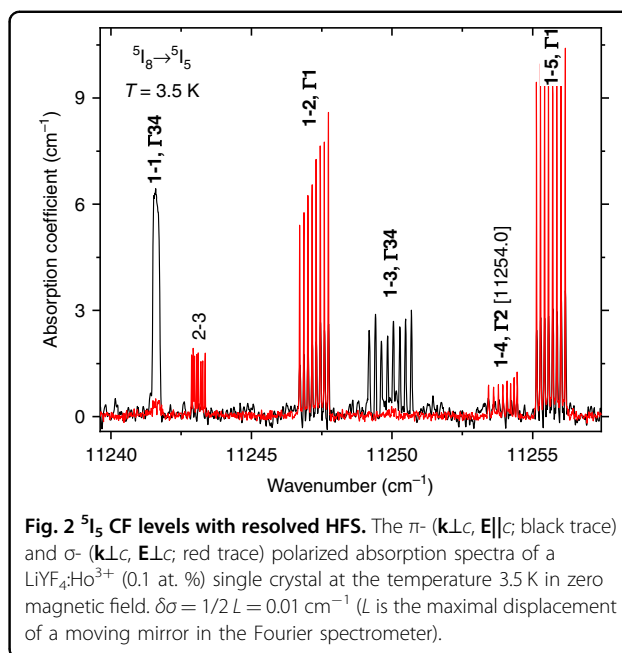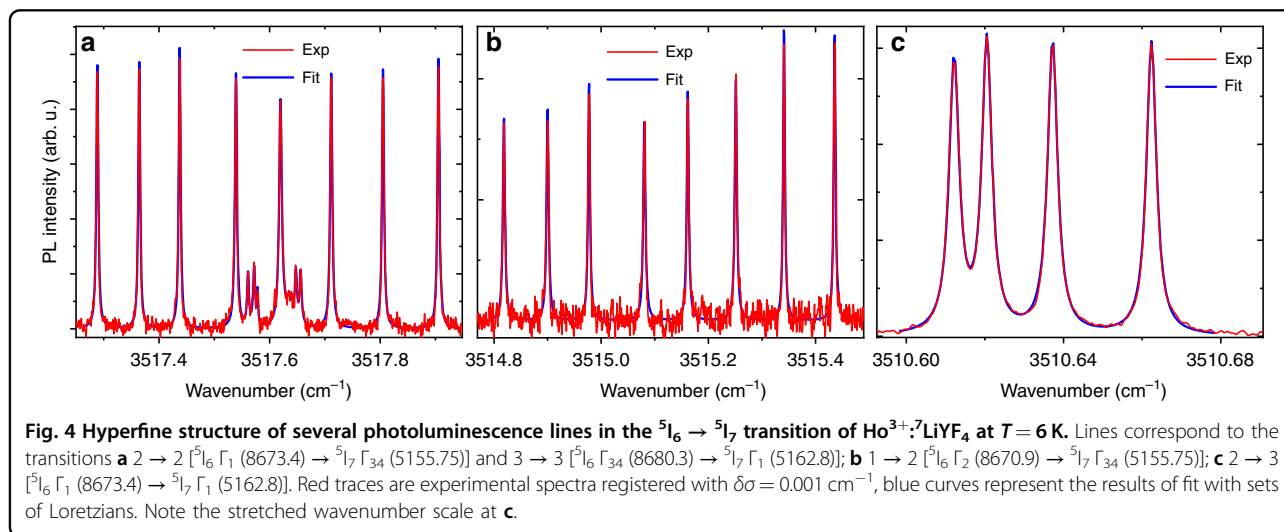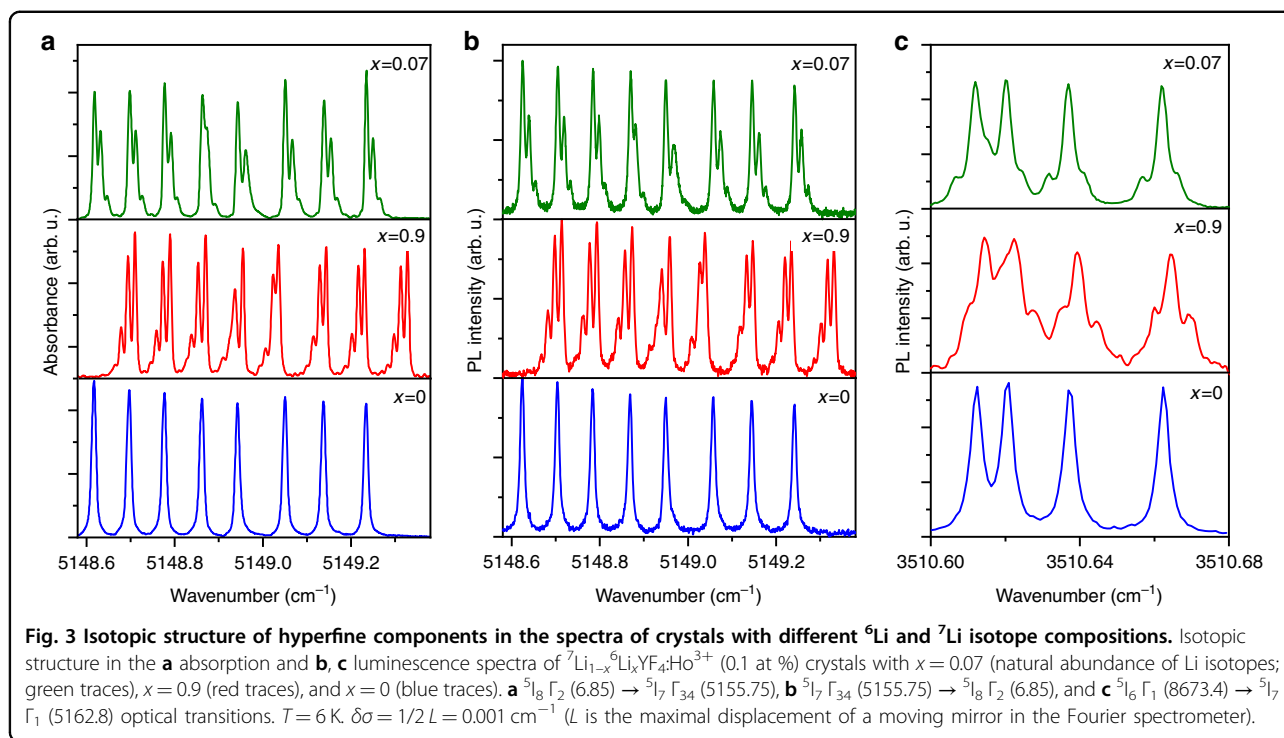
Fig. 3 Isotopic structure of hyperfine components in the spectra of crystals with different ^{6}Li and ^{7}Li isotope compositions. Isotopic structure in the **a** absorption and **b**, **c** luminescence spectra of ^{7}Li$_{1-x}$^{6}Li$_x$YF$_4$:Ho^{3+} (0.1 at %) crystals with $x = 0.07$ (natural abundance of Li isotopes; green traces), $x = 0.9$ (red traces), and $x = 0$ (blue traces). **a** ^{5}I$_8$ Γ_2 (6.85) → ^{5}I$_7$ Γ_{34} (5155.75), **b** ^{5}I$_7$ Γ_{34} (5155.75) → ^{5}I$_8$ Γ_2 (6.85), and **c** ^{5}I$_6$ Γ_1 (8673.4) → ^{5}I$_7$ Γ_1 (5162.8) optical transitions. $T = 6$ K. $\delta\sigma = 1/2 L = 0.001$ cm^{-1} (L is the maximal displacement of a moving mirror in the Fourier spectrometer).

Fig. 4 Hyperfine structure of several photoluminescence lines in the ^{5}I$_6$ → ^{5}I$_7$ transition of Ho^{3+}:^{7}LiYF$_4$ at $T = 6$ K. Lines correspond to the transitions **a** 2 → 2 [^{5}I$_6$ Γ_1 (8673.4) → ^{5}I$_7$ Γ_{34} (5155.75)] and 3 → 3 [^{5}I$_{34}$ (8680.3) → ^{5}I$_7$ Γ_1 (5162.8)]; **b** 1 → 2 [^{5}I$_6$ Γ_2 (8670.9) → ^{5}I$_7$ Γ_{34} (5155.75)]; **c** 2 → 3 [^{5}I$_6$ Γ_1 (8673.4) → ^{5}I$_7$ Γ_1 (5162.8)]. Red traces are experimental spectra registered with $\delta\sigma = 0.001$ cm^{-1}, blue curves represent the results of fit with sets of Loretzians. Note the stretched wavenumber scale at **c**.
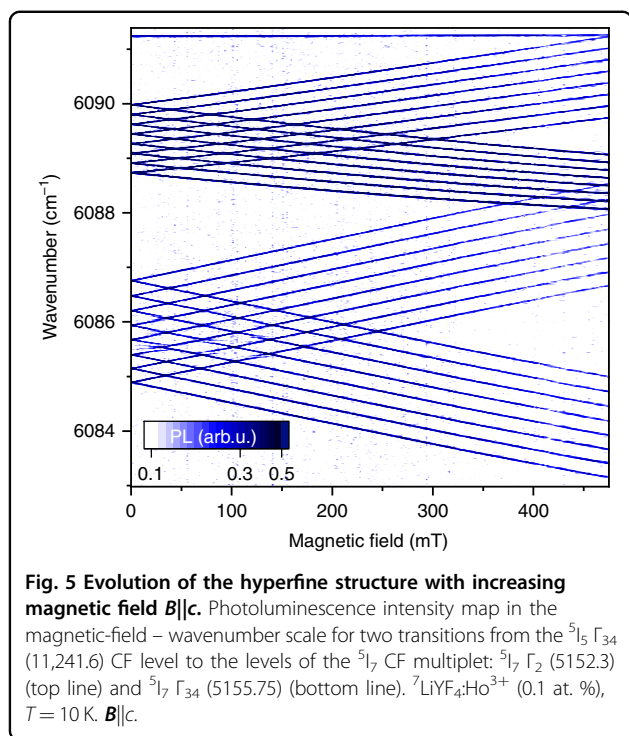
$g_{||}(11,241.6) + g_{||}(5155.75) = 8.1 + 6.8 = 14.9$ (see Supplementary information for more details; Supplementary Figs. S4–S34 show the magnetic-field-dependent PL spectra used to obtain the data given in Table 1).

Hyperfine levels' anticrossing in the photoluminescence spectra of ^{7}LiYF$_4$:Ho^{3+} in a magnetic field $B||c$

Figure 6a presents the PL intensity map for the radiative transition from the lowest electronic doublet in the ^{5}I$_7$ CF multiplet, ^{5}I$_7$ Γ_{34} (5155.75 cm^{-1}), to the first excited singlet of the ground ^{5}I$_8$ CF multiplet, ^{5}I$_8$ Γ_2 (6.85 cm^{-1}). The presented picture coincides with the one observed in the absorption spectra at the corresponding transition[33] and demonstrates gaps at the anticrossings of the |Γ_4, m> and |Γ_3, $m \pm 2$> states (|Δm| = 2) (see, e.g., a "huge" gap at 5149.0 cm^{-1} in Fig. 6a) and of the |Γ_4, m> and |Γ_3, m> states (|Δm| = 0). However, it should be noted that when measuring luminescence, a better contrast is achieved.

Narrowest PL lines of ^{7}LiYF$_4$:Ho^{3+} (0.1 at. %) in a magnetic field were observed in the case of the ^{5}I$_6$ → ^{5}I$_7$

Fig. 5 Evolution of the hyperfine structure with increasing magnetic field $B||c$. Photoluminescence intensity map in the magnetic-field – wavenumber scale for two transitions from the $^5I_5$ Γ_{34} (11,241.6) CF level to the levels of the $^5I_7$ CF multiplet: $^5I_7$ Γ_2 (5152.3) (top line) and $^5I_7$ Γ_{34} (5155.75) (bottom line). ^{7}LiYF$_4$:Ho^{3+} (0.1 at. %), $T = 10$ K. $B||c$.

transitions, the same as in a zero magnetic field. Figure 6b shows a representative example. Here, the spectrum of the $^5I_6$ Γ_2 (8670.9) $\rightarrow$ $^5I_7$ Γ_{34} (5155.75) transition is shown. This transition in the spectral region of 2.84 μm involves the same $^5I_7$ Γ_{34} (5155.75) CF doublet as the transition at 1.94 μm presented in Fig. 6a. Although the singlets participating in the transitions [$^5I_8$ Γ_2 (6.85 cm^{-1}) in the case of Fig. 6a and $^5I_6$ Γ_2 (8670.9) in the case of Fig. 6b] are different, the spectra are similar.

Figure 6c shows a fragment of the spectrum corresponding to the $^5I_6$ Γ_2 (8670.9) $\rightarrow$ $^5I_7$ Γ_{34} (5155.75) transition of ^{7}LiYF$_4$:Ho^{3+} (0.1 at. %) in a zero magnetic field and in the field of 140 mT at one of the anticrossings. A four-component structure at the $|\Delta m| = 2$ anticrossings and a very specific line shape at the $\Delta m = 0$ anticrossing are observed.
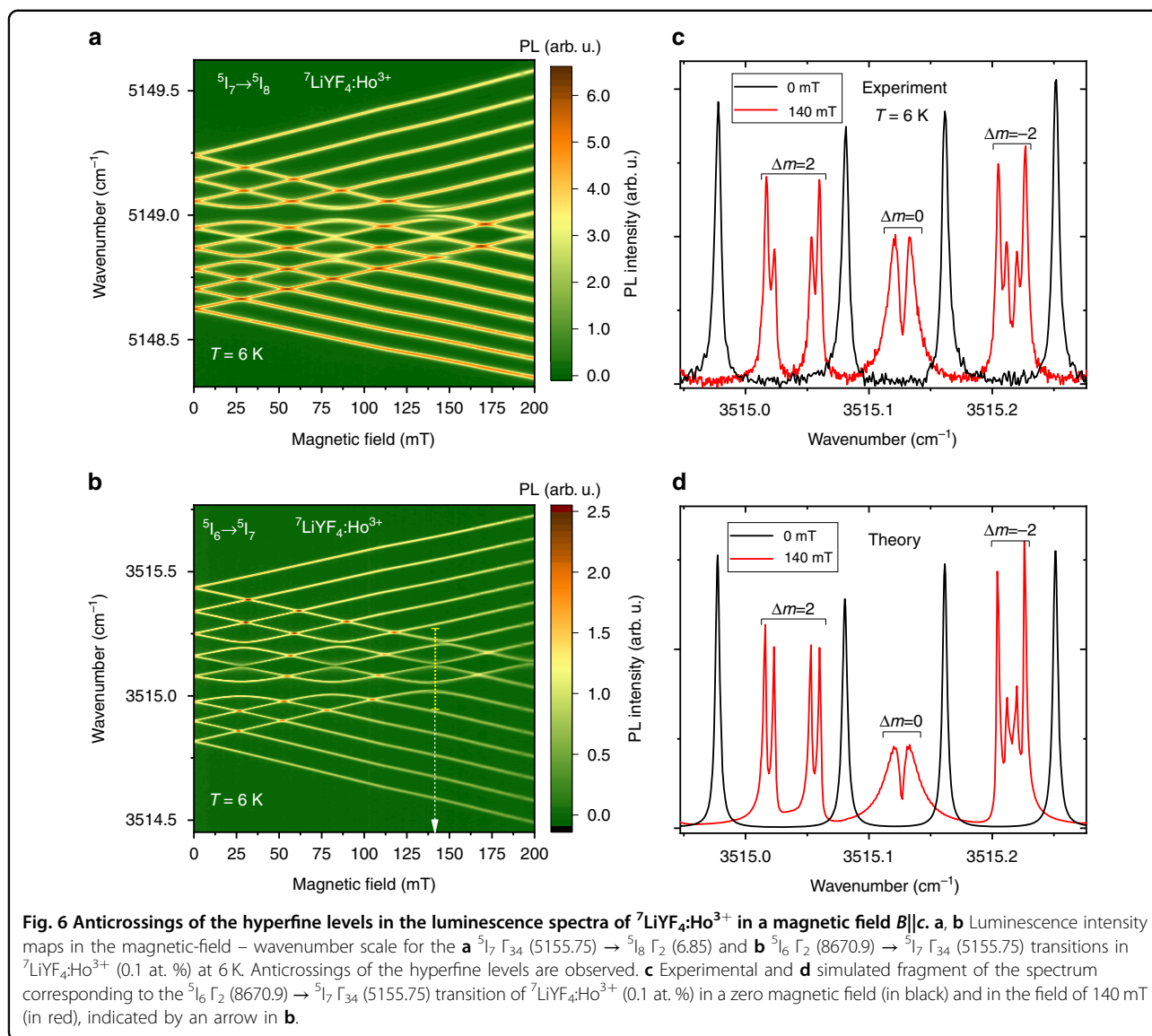
The $^5F_5$ Γ_{34} (15,495.4) CF level demonstrates the largest $\Delta m = 0$ gaps, which are observed in all the lines starting from this level. As an example, Fig. 7a shows the spectrum of the $^5F_5$ Γ_{34} (15,495.4) $\rightarrow$ $^5I_6$ Γ_2 (8670.9) transition. A large central gap is clearly seen in the hyperfine pattern in a magnetic field.

Discussion

Luminescence spectra complement absorption spectra, providing information on levels inaccessible to absorption. In the case of spectra consisting of narrow lines, the signal-to-noise ratio in PL spectra is much higher than in absorption spectra. Moreover, in some cases, the PL lines are noticeably narrower than the absorption ones, so that

the HFS is resolved much better. A good example can be found in Fig. 4, where, in particular, quadrupole HFS of a $\Gamma_1 \rightarrow \Gamma_1$ magnetic dipole transition is observed (Fig. 4c, see Supplementary Table S1 for selection rules). The use of luminescence instead of absorption makes it possible to work with micron- or even nano-sized samples, which is important, e.g., for sensor applications. The PL spectra of LiYF$_4$:Ho^{3+} can be used to control the external magnetic field. Here, the $^5F_5 \rightarrow ^5I_6$ and $^5I_5 \rightarrow ^5I_7$ luminescent transitions near 1.64 and 1.46 μm, respectively, fall into the transparency window of optical fibers and offer a possibility to implement, for example, remote magnetic field sensors. Let us consider the PL line at 6085.85 cm^{-1} [$^5I_5$ Γ_{34} (11241.6) $\rightarrow$ $^5I_7$ Γ_{34} (5155.75), see Fig. 5], the magnetic-field splitting of which, $\Delta = \mu_B g_{||} B$ (see Supplementary Eq. S4), follows the sum of g factors of the levels involved: $g_{||} = g_{||}(11,241.6) + g_{||}(5155.75) = 14.9$. The position of a spectral line with the known shape can be determined with an accuracy δσ equal to 0.1 FWHM of the instrumental function[34] (in Fourier spectroscopy, where the wavenumber scale over the entire spectral region is set by a stabilized He-Ne laser, this is also the accuracy of the absolute wavenumber scale[35]). In our case, the instrumental function is characterized by FWHM $= 0.6/2 L$. For $L = 500$ cm we find δσ $= 0.6 \cdot 10^{-4}$ cm^{-1}. Using the relation δΔ $= 2$δσ $= \mu_B g_{||}$δB, one obtains δB $= 17$ μT, i.e., the strength of an external magnetic field can be determined with the precision δB ≈ 17 μT. It is worth noting that the range of measured magnetic fields can be very broad (calibration curve σ(B) can be used for strong fields, for which Supplementary Eq. S4 is not valid). It is also possible to determine the direction of the magnetic field by installing two LiYF$_4$:Ho crystals with the mutually perpendicular c axes ($g_\perp = 0$ for non-Kramers doublets). To control small deviations of the magnetic field strength, the method developed for magnetometry with nitrogen-vacancy (NV) centers in diamond[36] can be applied. In ref. [36], a field-dependent position of a dip in the NV luminescence intensity was controlled with an accuracy of ~μT using AOM-modulated laser excitation and a lock-in amplifier. The authors of ref. [36] noted that their "technique can be extended to other magnetically sensitive features in the NV PL or absorption, as well as features associated with other spin defects in solid-state systems". In particular, a narrow hyperfine component in the luminescence spectrum of ^{7}LiYF$_4$:Ho^{3+} can be used instead of a dip in a broad luminescence spectrum of NV. Unlike the case of NV centers[36], no additional field (102.4 mT, to set at the ground-state level anticrossing, and a secondary coil to apply small modulation of this field) is necessary in the case of LiYF$_4$:Ho, which can be favorable for quantum technology devices.

Similar to a ruby luminescent pressure sensor, a small piece of LiYF$_4$:Ho crystal can be placed nearby a quantum-memory crystal in the repeater, operating at

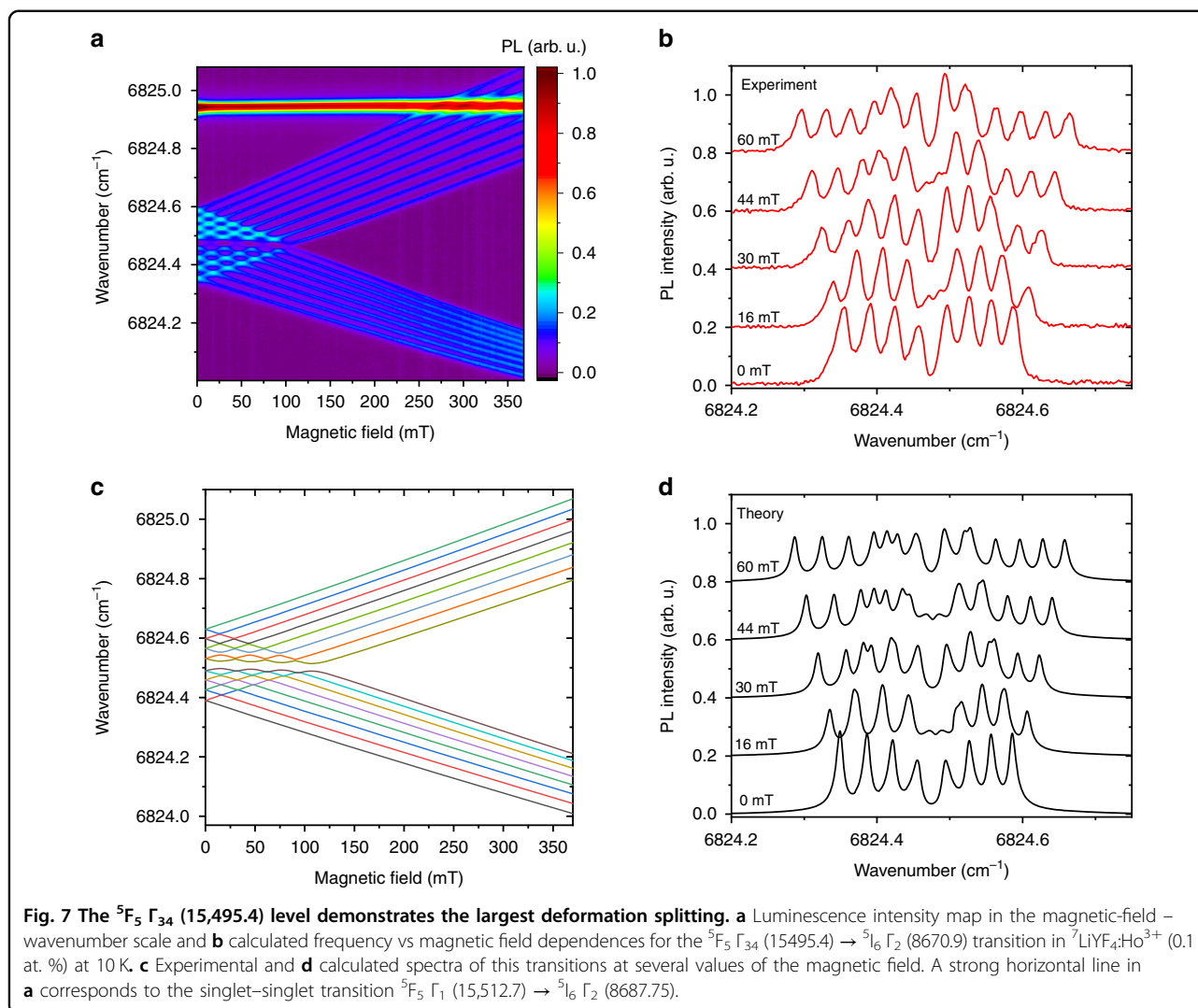**Fig. 6 Anticrossings of the hyperfine levels in the luminescence spectra of $^7LiYF_4:Ho^{3+}$ in a magnetic field $B||c$. a, b** Luminescence intensity maps in the magnetic-field – wavenumber scale for the **a** $^5I_7$ Γ_{34} (5155.75) → $^5I_8$ Γ_2 (6.85) and **b** $^5I_6$ Γ_2 (8670.9) → $^5I_7$ Γ_{34} (5155.75) transitions in $^7LiYF_4:Ho^{3+}$ (0.1 at. %) at 6 K. Anticrossings of the hyperfine levels are observed. **c** Experimental and **d** simulated fragment of the spectrum corresponding to the $^5I_6$ Γ_2 (8670.9) → $^5I_7$ Γ_{34} (5155.75) transition of $^7LiYF_4:Ho^{3+}$ (0.1 at. %) in a zero magnetic field (in black) and in the field of 140 mT (in red), indicated by an arrow in **b**.

low temperatures, to control an external magnetic field used to adjust the energy levels. However, the implementation of a practical and convenient sensor requires additional work. A high-resolution Fourier spectrometer, being the only spectral instrument able to deliver information on the HFS in a wide spectral range, is a bulky and very expensive device. A possible solution to the problem is to isolate the desired spectral line with an interference filter and use a Fabry–Perot interferometer. To avoid overlay of the interference orders, the free spectral range should be $2\,cm^{-1}$, which dictates a distance between Fabry–Perot mirrors 2.5 mm. In order to obtain a resolution of about $0.002\,cm^{-1}$ in this case, it is necessary to have a finesse of about 1000. The finesse depends on the reflection coefficient of the mirrors and the quality of their surface. Currently, firms offer

Fabry–Perot interferometers with finesse up to 1500 in a wide spectral range[37].

Monoisotopic crystals are most favorable for realizing sensitive sensors, because they demonstrate the narrowest lines (as Fig. 3 convincingly shows). On the other hand, the isotopic structure in the spectra of $LiYF_4:Ho^{3+}$ reflects the lithium isotope composition in a crystal. Under neutron irradiation, the ^6Li isotopes can capture neutrons converting to ^7Li. A change of the isotope composition in a crystal originally enriched with the ^6Li isotope could be detected by PL spectra.

Next, we turn to the anticrossings observed in the PL spectra. As was shown in ref. [33] on the basis of magnetic-field-dependent absorption spectra of $^7LiYF_4:Ho^{3+}$, gaps observed at the anticrossings of the $|\Gamma_4, m>$ and $|\Gamma_3, m \pm 2>$ states ($|\Delta m| = 2$) are caused by the transverse term in

Fig. 7 The $^5F_5$ Γ_{34} (15,495.4) level demonstrates the largest deformation splitting. a Luminescence intensity map in the magnetic-field – wavenumber scale and **b** calculated frequency vs magnetic field dependences for the $^5F_5$ Γ_{34} (15495.4) $\rightarrow$ $^5I_6$ Γ_2 (8670.9) transition in ^{7}LiYF$_4$:Ho^{3+} (0.1 at. %) at 10 K. **c** Experimental and **d** calculated spectra of this transitions at several values of the magnetic field. A strong horizontal line in **a** corresponds to the singlet–singlet transition $^5F_5$ Γ_1 (15,512.7) $\rightarrow$ $^5I_6$ Γ_2 (8687.75).

magnetic dipole hyperfine interaction but the four-component structure at the $|\Delta m| = 2$ anticrossings arises due to the mixing of the electron-nuclear wave functions of the crossing levels in the vicinity of the anticrossing point (at the anticrossing point, the wave functions of the crossing levels are present with equal weights). The $\Delta m = 0$ gaps have a different nature, they are due to random crystal-lattice deformations always present in a real crystal[33]. Here, we focus on anticrossings of the hyperfine levels with equal nuclear spin projections, $\Delta m = 0$, which can be used to check crystal quality. In particular, by analyzing PL of Ho^{3+} (either introduced in a small amount or present as uncontrolled impurity) in ^{7}LiYF$_4$:Nd, one can check the quality of this crystal proposed[7] for a quantum memory based on off-resonant Raman interaction.

A very specific line shape with a sharp dip in the center and slopy wings is especially well seen just in the luminescence spectra (see Fig. 6c). Previously, such line shape was observed for electronic transitions between singlet

and doublet CF levels in the spectra of LiYF$_4$:Tm^{3+} (ref. [23]), Cs$_2$NaYF$_6$:Yb^{3+} (ref. [31]), and Tm^{3+} in ABO$_4$ (A = Y, Lu; B = P, V)[32] and was shown to be the result of random lattice deformations[23,31,32]. A theory has been developed that made it possible to extract information about the strain distribution function from the analysis of the line shape[32]. The measured shape of the PL line with a dip at the center in the region of the $\Delta m = 0$ anticrossings for the singlet-doublet transition $^5I_6$ Γ_2 (8670.9) $\rightarrow$ $^5I_7$ Γ_{34} (5155.7) is modeled here on the basis of this theory.

The Hamiltonian of the electronic 4f^{10} shell of the Ho^{3+} impurity ion, $H = H_{FI} + H_{CF} + V$, where $V = H_{MHF} + H_{QHF} + H_Z + H_{EID}$, contains the free-ion energy H_{FI}, the interaction with the crystal-field H_{CF}, the magnetic (H_{MHF}) and quadrupole (H_{QHF}) hyperfine interactions, the electronic and nuclear Zeeman energies H_Z in an external magnetic field, and the electron-deformation interaction H_{EID}, linear in components $e_{\alpha\beta}$ of the strain tensor $\boldsymbol{e}$. Modeling of the spectral profiles involves

consequent numerical diagonalizations of the Hamiltonian $H_0 = H_{\mathrm{FI}} + H_{\mathrm{CF}}$ defined in the total space of 1001 electronic states and, at the next step, of the projection of the operator V onto the truncated basis of $76 \times 8 = 608$ electron-nuclear states corresponding to the lower 76 eigenvalues (E_Γ) of the Hamiltonian H_0. The obtained energies $E_{\Gamma j}$ and wave functions of the electron-nuclear sublevels of the ^5I_J ($J = 4,...8$) and $^5F_5$ multiplets are used to calculate intensity distributions in spectral lines corresponding to magnetic (electric) dipole radiative transitions $\Gamma \rightarrow \Gamma'$ at fixed values of the magnetic field strength and strain tensor components,

$$I_{\Gamma\Gamma'}(E, \mathbf{e}) = \sum_{j \in \Gamma} \sum_{k \in \Gamma'} \sum_\alpha |\langle \Gamma' k | M_\alpha | \Gamma j \rangle|^2 I_{0,\Gamma\Gamma'}(E_{\Gamma j} - E_{\Gamma' k} - E)$$

(1)

Here M is the magnetic (electric) dipole moment operator of ten 4f electrons and $I_{0,\Gamma\Gamma'}(x) = (\delta E_{\Gamma\Gamma'}/\pi)(x^2 + \delta E_{\Gamma\Gamma'}^2)^{-1}$ is the form-function with FWHM $2\delta E_{\Gamma\Gamma'}$ of individual transitions between hyperfine sublevels of the CF states Γ and Γ'. Note that for the intraconfigurational transitions, the structure of the effective even electric dipole moment operator is determined by the odd component of the crystal field. The finite spectral envelope is modeled by averaging the distribution (1) with the distribution function $g(\mathbf{e})$ of random strains induced by lattice point defects in LiYF$_4$ crystals, taking into account the elastic anisotropy of the crystal lattice[32]. The most pronounced spectral effect of random strains, namely, the formation of a dip in the envelope of the transition involving a CF non-Kramers doublet Γ_{34}, is caused by rhombic strains $e(B_g^1) = (e_{xx} - e_{yy})/2$ and $e(B_g^2) = e_{xy}$, which transform according to the B_g IR of the C_{4h} lattice factor group and split Γ_{34} doublets. The corresponding distribution function can be written as follows:

$$g\left(e\left(B_g^1\right), e\left(B_g^2\right)\right) = \frac{\nu_{B_g}\gamma_{B_g}}{2\pi}\left(\nu_{B_g}^2 e_1^2 + e_2^2 + \gamma_{B_g}^2\right)^{-3/2}$$

(2)

where $\nu_{B_g} = 2.44$, $e_1 = e(B_g^1)\cos\varphi - e(B_g^2)\sin\varphi$, $e_2 = e(B_g^1)\sin\varphi + e(B_g^2)\cos\varphi$, $\varphi = 28.7°$ (ref. [32]), and γ_{B_g}, which is proportional to the concentration of defects and determines the distribution width, is considered as a fitting parameter.

Experimental shapes of spectral lines were satisfactorily reproduced by computations of integrals over a two-dimensional space of random strains ($x = e(B_g^1), y = e(B_g^2)$)

$$I_{\Gamma\Gamma'}(E) \sim \iint I_{\Gamma\Gamma'}(E, x, y)g(x, y)dxdy$$

(3)

where we used $\gamma_{B_g} = 5 \cdot 10^{-5}$ and parameters of the electron-deformation interaction presented in ref. [33]. Examples of the obtained spectral envelopes in external

magnetic fields (including fields with strengths corresponding to the $\Delta m = \pm 2$ and $\Delta m = 0$ anticrossings) are shown in Figs. 6d and 7d.

In summary, we have presented the first observation of the resolved hyperfine structure in the luminescence spectra of a RE-doped crystal and demonstrated PL lines as narrow as 0.002–$0.004\,\mathrm{cm}^{-1}$ and with magnetic g factors as large as 10–15, including in the telecommunication spectral range. These PL lines are promising for creating remote magnetic field sensors that do not require an additional constant or variable magnetic field and/or microwave field and are capable of operating in a very wide range of measured magnetic fields. Our results pave the way for the development of a remote magnetic field sensor for, e.g., quantum repeaters installed in an extended quantum communication line. This work is also the first observation of hyperfine levels anticrossings in the luminescence spectra. The $\Delta m = 0$ anticrossings can be used to evaluate random lattice deformations in crystals for quantum information devices, i.e., the crystal quality.

Materials and methods
Crystal growth

Three single crystals of LiYF$_4$:Ho (0. 1 at. %) with different content of ^{7}Li and ^{6}Li isotopes were grown by the Stockbarger method. Li$_2$CO$_3$ with known lithium isotope composition was taken as a starting material. It was transformed into LiF by the "dry" method. The crystals were then grown from the mixture of appropriate fluorides. Samples with dimensions $3 \times 3 \times 8\,\mathrm{mm}^3$ and containing the c axis in the $3 \times 3\,\mathrm{mm}^2$ plane were cut from the x-ray oriented crystals and polished.

Optical spectroscopy and low-temperature measurements

In the PL experiments displayed in Fig. 1a, a LiYF$_4$:Ho^{3+} sample was placed into a cryomagnetic system (**1**) of our own design based on a Sumitomo RP096 closed-cycle helium cryostat. The design feature was that the electromagnet together with the concentrating magnetic system was attached directly to the first stage of the cryostat, which reduced the system dimensions, eliminated the need for heat removal in a vacuum, and allowed the use of higher currents and, consequently, magnetic fields, as the resistivity of copper winding wires was significantly reduced. A computer-controlled multi-channel current source Korad KA3305P (**1b**) was used to change the magnitude of the applied magnetic field. The magnetic field was directed along the c axis of the crystal and could be varied from 0 to 500 mT. The sample temperature was chosen such that several lower CF levels of each excited CF multiplet were populated, but the spectral lines were not yet broadened due to the electron–phonon interaction, and were set in the range from 3.5 to 10 K. The

temperature was measured with a Si-diode temperature sensor (Scientific Instruments Si-410-AA) and a temperature controller (Lakeshore 335) (**1a**) and was stabilized with the precision of ±0.05 K during the entire measurement period. Emission was excited by the linearly polarized light of a diode laser (Oclaro HL63193) with 100 mW power, incident perpendicular to the *c* axis of the crystal and polarized along the *c* axis; the spot on the crystal was 0.5 mm. The laser wavelength could be changed in the interval 635 ± 10 nm by changing the temperature in the range from $t = -20$ to $+45\,°C$ using a self-made thermoelectric cooler and resistive heater. The laser temperature $+36.4\,°C$ was chosen by searching for the maximum PL signal. A homemade temperature stabilization system with feedback (**2a**) based on a temperature controller Scientific Instruments M9700 was implemented. Thus selected laser wavelength 638.3 nm excited the upper CF level of the $^5F_5$ multiplet (Supplementary Fig. S1). Emission from the crystal was collimated by a mirror (diameter 90 mm, focal length 418 mm) in a homemade evacuated (10^{-6} Torr) PL module (**3**) separated from a Fourier spectrometer (**4**) by a CaF_2 window W1. This gave a possibility of recording the spectra in the region of the atmospheric absorption in the middle and far infrared. Emission spectra were registered on a Bruker IFS 125HR high-resolution vacuum Fourier spectrometer (**4**) in the wavenumber range $2500–16,000\,cm^{-1}$, with the maximal displacement of a moving mirror in the Michelson interferometer up to $L = 500$ cm, which provided the instrumental function with $FWHM = 0.6\ \delta\sigma$, where $\delta\sigma = 1/2\,L = 0.001\,cm^{-1}$ (see Supplementary Eq. S2). Thus, the minimal width of the instrumental function used to register PL spectra was $0.0006\,cm^{-1}$ (18 MHz). The smallest input diaphragm D used was 0.3 mm in diameter. Polarized PL spectra were measured using a BaF_2 crystal-based polarizer for the mid- and near-infrared ranges. Radiation from the output of the Michelson interferometer was directed to a homemade registration module (**5**) separated from the spectrometer by a CaF_2 window W2, with an optical cutoff filter F to eliminate excitation laser light [Semrock single notch filter NF03-633E or a germanium plate (red in Fig. 1a)]. Depending on the studied region of the spectrum, highly sensitive detectors based on InSb ($1800–5500\,cm^{-1}$), high-gain InGaAs ($5500–9000\,cm^{-1}$), or SiPM ($9000–15,500\,cm^{-1}$) semiconductors were used. The signal was amplified by preamplifiers of our own design and then fed to the 16-bit ADC of the spectrometer (**5a**). The spectrum was calculated as a Fourier transform of the interferogram on a workstation (**6**) equipped with Bruker OPUS™ software, LabView™ software, and homemade software modules for COM ports that monitor and change sample and diode laser temperatures and electromagnet current. Polarized absorption spectra in zero magnetic field were acquired on the same experimental setup.

Author contributions
K.N.B. and M.N.P. conceived the experiments. K.N.B. designed and built the luminescence module of the setup and conducted the experiments. M.N.P. analyzed the results of measurements, identified the spectral lines, and interpreted the hyperfine structures. B.Z.M. performed the crystal-field calculations and luminescence spectra modeling, taking into account random lattice strains. K.N.B. prepared the figures. M.N.P. wrote the manuscript with discussion with B.Z.M. and K.N.B. All authors contributed to the manuscript, reviewed it, and approved the submission of the final version of the manuscript.

Data availability
The data that support the plots within the paper and other findings of this study are available from the corresponding author upon reasonable request.

References
1. Kolesnikov, I., & Manshina, A. Rare earth ion based luminescence thermometry. In *Progress in Photon Science* (eds Yamanouchi, K., Manshina, A. A. & Makarov, V. A.) 69–94 (Chem, Springer, 2021). https://doi.org/10.1007/978-3-030-77646-6_5
2. Yu, D. et al. One ion to catch them all: targeted high-precision Boltzmann thermometry over a wide temperature range with Gd^{3+}. *Light Sci. Appl.* **10**, 236, https://doi.org/10.1038/s41377-021-00677-5 (2021).
3. Thiel, C. W., Böttger, T. & Cone, R. L. Rare-earth-doped materials for applications in quantum information storage and signal processing. *J. Lumin.* **131**, 353–361, https://doi.org/10.1016/j.jlumin.2010.12.015 (2011).
4. Goldner, P., Ferrier, A. & Guillot-Noël, O. Rare-earth-doped crystals for quantum information processing. *Handb. Phys. Chem. Rare Earths* **46**, 1–78, https://doi.org/10.1016/B978-0-444-63260-9.00267-4 (2015).
5. Heshami, K. et al. Quantum memories: emerging applications and recent advances. *J. Mod. Opt.* **63**, 2005–2028, https://doi.org/10.1080/09500340.2016.1148212 (2016).
6. Ahlefeldt, R. L., Hush, M. R. & Sellars, M. J. Ultranarrow optical inhomogeneous linewidth in a stoichiometric rare-earth crystal. *Phys. Rev. Lett.* **117**, 250504, https://doi.org/10.1103/PhysRevLett.117.250504 (2016).
7. Akhmedzhanov, R. et al. Electromagnetically induced transparency in an isotopically purified Nd^{3+}:YLiF$_4$ crystal. *Phys. Rev. B* **97**, 245123, https://doi.org/10.1103/PhysRevB.97.245123 (2018).
8. Stuart, J. S., Hedges, M., Ahlefeldt, R. & Sellars, M. Initialization protocol for efficient quantum memories using resolved hyperfine structure. *Phys. Rev. Res.* **3**, L032054, https://doi.org/10.1103/PhysRevResearch.3.L032054 (2021).
9. Agladze, N. I. & Popova, M. N. Hyperfine structure in optical spectra of LiYF$_4$-Ho. *Solid State Commun.* **55**, 1097–1100, https://doi.org/10.1016/0038-1098(85)90141-3 (1985).
10. Agladze, N. I., Vinogradov, E. A. & Popova, M. N. Manifestation of quadrupole hyperfine interaction and of interlevel interaction in the optical spectrum of the LiYF$_4$:Ho crystal. *Sov. Phys. JETP* **64**, 716–720 (1986).

11. Popova, M. N. & Agladze, N. I. Hyperfine structure in optical spectra of LiYF4-Ho^{3+}: forbidden transitions. *Mol. Phys.* **102**, 1315–1318, https://doi.org/10.1080/00268970410001728618 (2004).

12. Matmon, G. et al. Optical response from terahertz to visible light of electron-nuclear transitions in LiYF$_4$:Ho^{3+}. *Phys. Rev. B* **94**, 205132, https://doi.org/10.1103/PhysRevB.94.205132 (2016).

13. Pytalev, D. S. et al. Hyperfine interactions of Ho^{3+} ions in KY$_3$F$_{10}$: electron paramagnetic resonance and optical spectroscopy studies. *Phys. Rev. B* **86**, 115124, https://doi.org/10.1103/PhysRevB.86.115124 (2012).

14. Baraldi, A. et al. Hyperfine interactions in YAB:Ho^{3+}: A high-resolution spectroscopy investigation. *Phys. Rev. B* **76**, 165130, https://doi.org/10.1103/PhysRevB.76.165130 (2007).

15. Shakurov, G. S. et al. Random strain effects in optical and EPR spectra of electron-nuclear excitations in CaWO$_4$:Ho^{3+} single crystals. *Phys. Chem. Chem. Phys.* **16**, 24727–24738, https://doi.org/10.1039/c4cp03437f (2014).

16. Wells, J.-P. et al. Hyperfine patterns of infrared absorption lines of Ho^{3+} C$_{4v}$ centres in CaF$_2$. *Mol. Phys.* **102**, 1367–1376, https://doi.org/10.1080/00268970410001728555 (2004).

17. Mazzera, M. et al. Hyperfine structure of Ho^{3+} levels and electron–phonon coupling in YPO$_4$ single crystals. *J. Phys.: Condens. Matter* **24**, 205501, https://doi.org/10.1088/0953-8984/24/20/205501 (2012).

18. Mothkuri, S. et al. Electron-nuclear interactions as a test of crystal field parameters for low-symmetry systems: Zeeman hyperfine spectroscopy of Ho^{3+}-doped Y$_2$SiO$_5$. *Phys. Rev. B* **103**, 104109, https://doi.org/10.1103/PhysRevB.103.104109 (2021).

19. Popova, M. N. et al. Experimental and theoretical study of the crystal-field levels, hyperfine and electron-phonon interactions in LiYF$_4$:Er^{3+}. *Phys. Rev. B* **61**, 7421, https://doi.org/10.1103/PhysRevB.61.7421 (2000).

20. Gerasimov, K. I. et al. High-resolution magneto-optical spectroscopy of ^{7}LiYF$_4$:^{167}Er^{3+}, ^{166}Er^{3+} and analysis of hyperfine structure of ultranarrow optical transitions. *Phys. Rev. B* **94**, 054429, https://doi.org/10.1103/PhysRevB.94.054429 (2016).

21. Popova, M. N. et al. Crystal field and hyperfine structure of ^{167}Er^{3+} in YPO$_4$:Er single crystals: high-resolution optical and EPR spectroscopy. *Phys. Rev. B* **99**, 235151, https://doi.org/10.1103/PhysRevB.99.235151 (2019).

22. Marino, R. et al. Energy level structure and optical dephasing under magnetic field in Er^{3+}:LiYF$_4$ at 1.5 μm. *J. Lumin.* **169**, 478–482, https://doi.org/10.1016/j.jlumin.2015.03.003 (2016).

23. Klimin, S. A. et al. High-resolution optical spectroscopy of Tm^{3+} ions in LiYF$_4$: crystal-field energies, hyperfine and deformation splittings, and the isotopic structure. *Phys. Rev. B* **81**, 045113, https://doi.org/10.1103/PhysRevB.81.045113 (2010).

24. Macfarlane, R. M., Meltzer, R. S. & Malkin, B. Z. Optical measurement of the isotope shifts and hyperfine and superhyperfine interactions of Nd in the solid state. *Phys. Rev. B* **58**, 5692–5700, https://doi.org/10.1103/PhysRevB.58.5692 (1998).

25. Akhmedzhanov, R. A. et al. Atomic frequency comb memory in an isotopically pure ^{143}Nd^{3+}:Y^{7}LiF$_4$ crystal. *Laser Phys. Lett.* **13**, 015202, https://doi.org/10.1088/1612-2011/13/1/015202 (2016).

26. Agladze, N. I. et al. Isotope structure in optical spectra of LiYF$_4$:Ho^{3+}. *Phys. Rev. Lett.* **66**, 477–480, https://doi.org/10.1103/PhysRevLett.66.477 (1991).

27. Agladze, N. I. et al. Isotope effects in the lattice structure and vibrational and optical spectra of ^{6}Li$_x$^{7}Li$_{1-x}$YF$_4$:Ho crystals. *J. Exp. Theor. Phys.* **77**, 1021–1033 (1993).

28. Macfarlane, R. M., Cassanho, A. & Meltzer, R. S. Inhomogeneous broadening by nuclear spin fields: a new limit for optical transitions in solids. *Phys. Rev. Lett.* **69**, 542–545, https://doi.org/10.1103/PhysRevLett.69.542 (1992).

29. Chukalina, E. P. et al. Fine structure of spectral lines in LiYF$_4$:Er^{3+} due to isotopic disorder in the lattice. *Phys. Lett. A* **269**, 348–350, https://doi.org/10.1016/S0375-9601(00)00273-5 (2000).

30. Kukharchyk, N. et al. Optical coherence of ^{166}Er:^{7}LiYF$_4$ crystal below 1 K. *N. J. Phys.* **20**, 023044, https://doi.org/10.1088/1367-2630/aaa7e4 (2018).

31. Malkin, B. Z. et al. Random lattice deformations in rare earth doped cubic hexafluoroelpasolites: High-resolution optical spectroscopy and theoretical studies. *Phys. Rev. B* **86**, 134110, https://doi.org/10.1103/PhysRevB.86.134110 (2012).

32. Malkin, B. Z. et al. Distribution function of random strains in an elastically anisotropic continuum and defect strengths of Tm^{3+} impurity ions in crystals with zircon structure. *Phys. Rev. B* **96**, 014116, https://doi.org/10.1103/PhysRevB.96.014116 (2017).

33. Boldyrev, K. N. et al. Direct observation of hyperfine level anticrossings in the optical spectra of a ^{7}LiYF$_4$:Ho^{3+} single crystal. *Phys. Rev. B* **99**, 041105, https://doi.org/10.1103/PhysRevB.99.041105 (2019). R.

34. Rautian, S. G. Real spectral apparatus. *Sov. Phys. Uspekhi* **66**, 245–273, https://doi.org/10.1070/PU1958v001n02ABEH003099 (1958).

35. Bell, R. J. *Introductory Fourier Transform Spectroscopy* (London, Academic Press, 2012).

36. Wickenbrock, A. et al. Microwave-free magnetometry with nitrogen-vacancy centers in diamond. *Appl. Phys. Lett.* **109**, 053505, https://doi.org/10.1063/1.4960171 (2016).

37. Thorlabs Products. *Scanning Fabry-Perot Interferometers [EB/OL]* https://www.thorlabs.com/newgrouppage9.cfm?objectgroup_id=859